Journal of Computational Physics 229 (2010) 8045–8063

Contents lists available at ScienceDirect

Journal of Computational Physics

journal homepage: www.elsevier.com/locate/jcp

Lattice Boltzmann simulations of micron-scale drop impact on dry surfaces

Taehun Lee *, Lin Liu

Department of Mechanical Engineering, City College of City University of New York, New York, NY 10031, USA

ARTICLE INFO

Article history:
Received 20 July 2009
Received in revised form 7 March 2010
Accepted 1 July 2010

Keywords:
Lattice Boltzmann method
Contact line dynamics
Parasitic currents
Drop impact

ABSTRACT

A lattice Boltzmann equation (LBE) method for incompressible binary fluids is proposed to model the contact line dynamics on partially wetting surfaces. Intermolecular interactions between a wall and fluids are represented by the inclusion of the cubic wall energy in the expression of the total free energy. The proposed boundary conditions eliminate the parasitic currents in the vicinity of the contact line. The LBE method is applied to micron-scale drop impact on dry surfaces, which is commonly encountered in drop-on-demand inkjet applications. For comparison with the existing experimental results [H. Dong, W.W. Carr, D.G. Bucknall, J.F. Morris, Temporally-resolved inkjet drop impaction on surfaces, AIChE J. 53 (2007) 2606–2617], computations are performed in the range of equilibrium contact angles from 31° to 107° for a fixed density ratio of 842, viscosity ratio of 51, Ohnesorge number (*Oh*) of 0.015, and two Weber numbers (*We*) of 13 and 103.

1. Introduction

The lattice Boltzmann equation (LBE) methods model two-phase flows by incorporating intermolecular interaction forces into the governing equations for the particle distribution functions, which essentially separate different phases and result in interfacial tension effects [1–7]. The intermolecular interaction forces are derived by minimization of the total free energy of the system. In the presence of the liquid–gas–solid triple contact line, the interaction between a liquid–gas interface and a solid surface is modeled by incorporating a wall free energy into the formulation of the total free energy in the form of a surface integral [8], although other treatments have been widely used [9–11].

Chang and Alexander [12], and Yan and Zu [13] employed Inamuro et al.'s LBE method for incompressible two-phase flows [5] to simulate spontaneous water drop spreading on both homogeneous and heterogeneous partially wetting surfaces. They assumed that the interactions between the fluid and the solid surface are of short-range [14], and thus can be modeled by a surface integral that appears in the boundary condition of the free energy [15]. Although the equilibrium profile of the spreading drops agreed well with prediction, no transient profiles were compared with either theory or experiment. Mukherjee and Abraham [16] investigated drop impact on dry surfaces whose equilibrium contact angles range from $\theta^{eq} = 35°$ to $\theta^{eq} = 150°$ using an axisymmetric, multiple-relaxation-time (MRT) LBE method. In their model, the effects of a solid surface on fluids are represented by introducing an external force field at the wall nodes. The strength of the external force was reported to be linearly proportional to the equilibrium static contact angle and tabulated for interpolation. When the contact line moves, as in drop spreading and recoil, the dynamic contact angle reconstructed from the "Hoffman's function" [17] and capillary number [18–20] was imposed as an input parameter in order to interpolate the values in the tabulated external force field. Both density and viscosity ratios were fixed at 10, which are significantly lower than most experimental

* Corresponding author. Tel.: +1 212 650 6122; fax: +1 212 650 8013.
E-mail address: thlee@ccny.cuny.edu (T. Lee).
URL: http://www1.ccny.cuny.edu/prospective/gsoe/faculty/lee_t.cfm (T. Lee).

0021-9991/$ - see front matter © 2010 Elsevier Inc. All rights reserved.
doi:10.1016/j.jcp.2010.07.007

conditions. Léopoldès et al. [21], Dupuis et al. [22], and Kusumaatma et al. [23] investigated spreading of droplets on chemically and topologically patterned substrates using the free energy approach [24,25].

A potentially important issue in the simulation of the contact line is the existence of the parasitic currents that become stronger in magnitude as the relative importance of interfacial tension outweighs other effects. As the characteristic length of the problem gets smaller, the interfacial tension starts to dominate over the volumetric forces, and the discretization error associated with the formulation of the interfacial tension increases, producing stronger parasitic currents that may lead to unphysical deformation of the contact line. Discretization of the interfacial forces at the fluid–solid interface is thus important in the accurate modeling of the micron-scale drop impact phenomenon. Recently, we have proposed wall boundary conditions for van der Waals fluids [26] based on the free energy approach [27]. Using the linear wall free energy, we showed that when the intermolecular force is formulated in the potential form and discretized with the isotropic finite difference, the parasitic currents in the region of the contact line of a static drop can be completely eliminated at equilibrium. In [26], however, no dynamic drops in contact with solid surfaces were studied and the liquid–vapor density ratio was fixed at 5 because of the intrinsic limitation of the linear wall free energy.

In this paper, a formulation of the LBE method for incompressible binary fluids [28] is presented and wall boundary conditions for both the particle distribution functions and the intermolecular forcing terms are proposed. The LBE method is applied to investigate micron-scale water drop impact on dry surfaces with different wettability. Understanding of micron-scale drop impact on a partially wetting solid surface is of great importance in the manufacturing of flat displays by ink jet printing and plastic electronics. Modeling micron-scale drop impact poses a challenge that originates from a relatively large capillary effect in the drop recoil stage. The computation results are compared with the experimental results by Dong et al. [29] for drop impact in the range of equilibrium contact angles θ^{eq}, from 31° to 150° for a fixed density ratio of 842, and a viscosity ratio of 51.

The paper is organized as follows. In Section 2, the Cahn–Hilliard model with advection is briefly reviewed and the cubic wall boundary condition is discussed. In Section 3, a systematic procedure to derive the LBEs for advective Cahn–Hilliard equation and for the pressure evolution and momentum equations is presented. Section 4 describes the discretizations of the LBE, spatial gradients, and boundary conditions. Validation of the present LBE method and the simulations of micron-scale drop impact on dry surfaces are presented in Section 5. Concluding remarks are given in Section 6.

2. Cahn–Hilliard model

The continuity equation for the species i of binary fluids can be written as [28,30]:

$$\frac{\partial \tilde{\rho}_i}{\partial t} + \nabla \cdot \tilde{\rho}_i \mathbf{u}_i = 0, \quad i = 1, 2, \tag{1}$$

where $\tilde{\rho}_i$ and $\mathbf{u}_i$ denote the local density and velocity of the species i, respectively. The mixture density, $\rho = \sum_{i=1}^{2} \tilde{\rho}_i$ is also conserved. For convenience, we choose the heavier fluid as the species 1. The local velocity $\mathbf{u}_i$ is related to the volume averaged velocity $\mathbf{u}$, the constant bulk density value ρ_i, and the volume diffusive flow rate $\mathbf{j}_i$ of component i by

$$\rho_i \mathbf{j}_i = \tilde{\rho}_i (\mathbf{u}_i - \mathbf{u}). \tag{2}$$

For the composition defined as $C = \tilde{\rho}_1 / \rho_1$, Eq. (1) can be rewritten as

$$\frac{\partial C}{\partial t} + \nabla \cdot (\mathbf{u} C) = -\nabla \cdot \mathbf{j}_1. \tag{3}$$

If the diffusive flow rate is not related to the densities but to the local compositions of two components, we have $\mathbf{j}_1 = -\mathbf{j}_2 = \mathbf{j}$, which yields [31]:

$$\nabla \cdot \mathbf{u} = 0. \tag{4}$$

The above condition is only approximately satisfied in the LBE method at low Mach number. The density may be taken as a linear function of the composition:

$$\rho = C\rho_1 + (1 - C)\rho_2. \tag{5}$$

In the advective Cahn–Hilliard equation, the diffusive flow rate is assumed to be proportional to the gradient of the chemical potential μ [30]:

$$\mathbf{j} = -M \nabla \mu, \tag{6}$$

where $M > 0$ is the constant mobility.

It is assumed that the interactions between the liquid–gas interface and the solid surface are of short-range and appear in a surface integral of the total free energy [8]. The total free energy then takes the following form:

$$\Psi_b + \Psi_s = \int_V \left(E_0(C) + \frac{\kappa}{2} |\nabla C|^2 \right) dV + \int_S \left(\phi_0 - \phi_1 C_s + \phi_2 C_s^2 - \phi_3 C_s^3 + \cdots \right) dS, \tag{7}$$

where the bulk energy is taken as $E_0 = \beta C^2(C-1)^2$ with β being a constant, κ is the gradient parameter, C_s is the composition at a solid surface that generally differs from the bulk or equilibrium composition, and ϕ_i with $i = 0, 1, 2, \ldots$ are constant coefficients. The equilibrium profile is determined such that the energy is minimized and reads $\mu = \mu_0 - \kappa\nabla^2 C = const$, in which $\mu_0 = \partial E_0/\partial C$ is the classical part of the chemical potential.

The plane interfacial profile at equilibrium is

$$C(z) = \frac{1}{2} + \frac{1}{2}\tanh\left(\frac{2z}{\xi}\right), \tag{8}$$

where z is the coordinate normal to the plane interface and ξ is the interface thickness. Given ξ and β, one can compute the gradient parameter $\kappa = \beta\xi^2/8$, and the interfacial tension between fluids:

$$\sigma_{21} = \int_0^1 \sqrt{2\kappa E_0(C)}\,dC = \frac{\sqrt{2\kappa\beta}}{6}. \tag{9}$$

The solution of Eq. (3) with Eq. (6) requires two boundary conditions. The boundary condition for $\nabla^2\mu$ ensures no mass flux due to the chemical potential gradient in the direction normal to the solid boundary:

$$\mathbf{n}\cdot\nabla\mu|_s = 0, \tag{10}$$

where $\mathbf{n}$ is the unit normal vector. The boundary condition for $\nabla^2 C$ can be established by minimizing the total free energy subject to the specified wall free energy.

Neglecting the terms higher than second-order in Ψ_s and minimizing the total free energy $\Psi_b + \Psi_s$ lead to the linear boundary condition [13,15]:

$$\mathbf{n}\cdot\nabla C|_s = -\frac{\phi_1}{\kappa}, \tag{11}$$

where

$$-\phi_1 = \pm\sqrt{2\kappa E_0(C_s)}. \tag{12}$$

Eq. (12) has four solutions, but there are only two stable solutions. If C represents the composition of the heavier fluid (fluid 1), the two stable solutions are expressed in terms of the dimensionless wetting potential $\Omega_1 = \phi_1/\sqrt{2\kappa\beta}$ as

$$C_{s,1} = \frac{1+\sqrt{1+\Omega_1}}{2}, \tag{13}$$

which is the composition of the heavier fluid in contact with a solid surface at equilibrium, and

$$C_{s,2} = \frac{1-\sqrt{1-\Omega_1}}{2}, \tag{14}$$

which is the composition of the lighter fluid in contact with a solid surface at equilibrium. The equilibrium contact angle θ^{eq} at the three-phase contact line is determined by considering Young's law:

$$\cos\theta^{eq} = \frac{(1+\Omega_1)^{3/2} - (1-\Omega_1)^{3/2}}{2}. \tag{15}$$

A detailed derivation of the linear boundary condition can be found in [13].

Notice that $C_{s,2} < 0$ on a non-wetting surface. Due to Eq. (5), a negative C_s results in a very small or even negative value of the equilibrium wall density, i.e., $\rho_{s,2} < 0$ if $C_{s,2} < (1 - \rho_1/\rho_2)^{-1}$. This indicates that as the density ratio ρ_1/ρ_2 increases, the value of the equilibrium wall density rapidly tends to zero and may turn negative even on a weakly non-wetting surface, triggering severe numerical instability. Yan and Zu [13] avoided negative density by postprocessing the computed density to be clamped between the two bulk fluid densities. However, such modification could introduce discontinuous stress field close to the contact line.

Negative equilibrium density on a non-wetting surface can fundamentally be avoided as the higher-order terms in Ψ_s are retained. To construct a cubic boundary condition, we neglect the interactions between the solid and bulk fluids and only take the interactions between the solid and fluid–fluid interface into consideration. This assumption leaves us the following choice of parameters; $\phi_0 = \phi_1 = 0$, $\phi_2 = 1/2\phi_c$, and $\phi_3 = 1/3\phi_c$, where ϕ_c is a constant to be determined. At equilibrium, we have two solutions, $C_{s,1} = 1$ and $C_{s,2} = 0$, that satisfy:

$$\phi_c\left(C_s - C_s^2\right) = \pm\sqrt{2\kappa E_0(C_s)}. \tag{16}$$

Irrespective of a degree of non-wettability, the positivity of $C_{s,2}$ is guaranteed at equilibrium and thus $\rho_{s,2}$ remains in the proximity of the bulk density ρ_2, although small fluctuations around the equilibrium value are expected in transient calculations.

The interfacial tension between the solid and fluids 1 and 2 are respectively obtained as

$$\sigma_{s1} = \phi_c\left(\frac{1}{2}C_{s,1}^2 - \frac{1}{3}C_{s,1}^3\right) + \int_{C_{s,1}}^{1}\sqrt{2\kappa E_0(C)}dC = \frac{\sqrt{2\kappa\beta}}{6}\Omega_c, \tag{17}$$

$$\sigma_{s2} = \phi_c\left(\frac{1}{2}C_{s,2}^2 - \frac{1}{3}C_{s,2}^3\right) + \int_{0}^{C_{s,2}}\sqrt{2\kappa E_0(C)}dC = 0, \tag{18}$$

for which the dimensionless wetting potential $\Omega_c = \phi_c/\sqrt{2\kappa\beta}$ is related to the equilibrium contact angle θ^{eq} due to Young's law:

$$\cos\theta^{eq} = \frac{\sigma_{s2} - \sigma_{s1}}{\sigma_{21}} = -\Omega_c. \tag{19}$$

This establishes the cubic boundary condition for $\nabla^2 C$:

$$\mathbf{n}\cdot\nabla C|_s = \frac{\phi_c}{\kappa}\left(C_s - C_s^2\right). \tag{20}$$

Once Eq. (20) is imposed, $\mu = \mu_0 - \kappa\nabla^2 C$ is treated as a scalar. The derivation of the cubic boundary condition for van der Waals fluids can be found in [32].

The composition C of bulk phase is allowed to slightly vary around 0 and 1 when the system is out of equilibrium. When the density ratio is large, this slight change in C may still result in very small density in the lighter fluid. Here we introduce an artificial free energy that acts as an obstacle to negative C:

$$E_A(C) = \begin{cases} \beta_A C^2, & \text{if} \quad C < 0, \\ 0, & \text{if} \quad C \geqslant 0. \end{cases} \tag{21}$$

Fig. 1 shows the profiles of typical bulk free energy E_0 and artificial free energy E_A, which is zero for $C \geqslant 0$ and increases more rapidly than E_0 for $C < 0$. The governing equation for the transport of C becomes:

$$\frac{\partial C}{\partial t} + \mathbf{u}\cdot\nabla C = M\nabla^2\hat{\mu}, \tag{22}$$

where $\hat{\mu} = \mu + \partial E_A/\partial C$. Since E_A is zero in the interfacial region and the heavier fluid, it does not affect the equilibrium state of the phase interface and its effect on the interfacial dynamics is negligible.

3. Discrete Boltzmann equations

The discrete Boltzmann equation (DBE) for the transport of the mixture density and momentum of incompressible binary fluids is given as follows [28,33–35]:

$$\frac{Df_\alpha}{Dt} = \left(\frac{\partial}{\partial t} + \mathbf{e}_\alpha\cdot\nabla\right)f_\alpha = -\frac{1}{\lambda}\left(f_\alpha - f_\alpha^{eq}\right) + \frac{1}{c_s^2}\left(\mathbf{e}_\alpha - \mathbf{u}\right)\cdot\mathbf{F}\Gamma_\alpha, \tag{23}$$

where f_α is the particle distribution function, $\mathbf{e}_\alpha$ is the α-direction microscopic particle velocity, ρ is the mixture density, $\mathbf{u}$ is the volume averaged velocity, c_s is the speed of sound, λ is the relaxation time, and f_α^{eq} is the equilibrium distribution function:

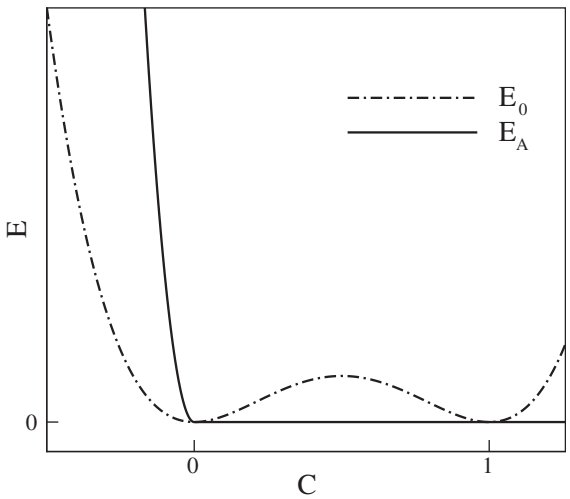

Fig. 1. Profiles of typical bulk energy E_0 and artificial energy E_A.

$$f_\alpha^{eq} = t_\alpha \rho \left[1 + \frac{\mathbf{e}_\alpha \cdot \mathbf{u}}{c_s^2} + \frac{(\mathbf{e}_\alpha \cdot \mathbf{u})^2}{2c_s^4} - \frac{(\mathbf{u}\cdot\mathbf{u})}{2c_s^2} \right] \tag{24}$$

with t_α being the weight [36], and $\Gamma_\alpha = \Gamma_\alpha(\mathbf{u}) = f_\alpha^{eq}/\rho$. The intermolecular force $\mathbf{F}$ comprises:

$$\mathbf{F} = \nabla \rho c_s^2 - (\nabla p - C\nabla\mu), \tag{25}$$

where ρc_s^2 is the ideal gas contribution to the pressure and p is the dynamic pressure that enforces the incompressibility. The total pressure is a sum of the dynamic pressure p, the thermodynamic pressure $C\mu_0 - E_0$, and the pressure due to the inclusion of curvature $-\kappa C\nabla^2 C + \frac{\kappa}{2}|\nabla C|^2$. In motionless flow, the contribution from p disappears, and the parasitic currents are eliminated.

Eq. (23) is the DBE for the *mass* and *momentum* equations and is to be transformed into the DBE for the *pressure evolution* and *momentum* equations. He et al. [4] first used the transformation to obtain the pressure evolution equation, although they did not make a distinction between the dynamic and thermodynamic pressures. We define a new particle distribution function:

$$g_\alpha = f_\alpha c_s^2 + (p - \rho c_s^2)\Gamma_\alpha(0), \tag{26}$$

and a new equilibrium distribution function:

$$g_\alpha^{eq} = f_\alpha^{eq} c_s^2 + (p - \rho c_s^2)\Gamma_\alpha(0) = t_\alpha \left[p + \rho c_s^2 \left(\frac{\mathbf{e}_\alpha \cdot \mathbf{u}}{c_s^2} + \frac{(\mathbf{e}_\alpha \cdot \mathbf{u})^2}{2c_s^4} - \frac{(\mathbf{u}\cdot\mathbf{u})}{2c_s^2} \right) \right]. \tag{27}$$

Taking the total derivative $D_t = \partial_t + \mathbf{e}_\alpha \cdot \nabla$ of the new variable g_α gives [28]:

$$\frac{\partial g_\alpha}{\partial t} + \mathbf{e}_\alpha \cdot \nabla g_\alpha = -\frac{1}{\lambda}(g_\alpha - g_\alpha^{eq}) + (\mathbf{e}_\alpha - \mathbf{u}) \cdot \left[\nabla \rho c_s^2 (\Gamma_\alpha - \Gamma_\alpha(0)) - C\nabla\mu\Gamma_\alpha \right], \tag{28}$$

where the dynamic pressure gradient is dropped because in the case of low Mach number ($Ma = |\mathbf{u}|/c_s$), the dynamic pressure is assumed to be $p \sim O(Ma^2)$, and $(\mathbf{e}_\alpha - \mathbf{u})\cdot\nabla p\ (\Gamma_\alpha - \Gamma_\alpha(0)) \sim O(Ma^3)$.

Eq. (28) recovers the pressure evolution equation:

$$\frac{\partial p}{\partial t} + \rho c_s^2 \nabla \cdot \mathbf{u} = 0, \tag{29}$$

and the momentum equation with the chemical potential gradient:

$$\rho \left(\frac{\partial \mathbf{u}}{\partial t} + \mathbf{u} \cdot \nabla \mathbf{u} \right) = -\nabla p - C\nabla\mu + \nabla \left[\rho c_s^2 \lambda \cdot \left(\nabla \mathbf{u} + (\nabla \mathbf{u})^T \right) \right], \tag{30}$$

where $\rho c_s^2 \lambda$ is identified as the dynamic viscosity η. Eq. (29) can be derived from the continuity equation. The dynamic pressure is related to the density by $\partial p/\partial\rho = c_s^2$, which leads to:

$$\frac{\partial p}{\partial t} + \rho c_s^2 \nabla \cdot \mathbf{u} + \mathbf{u} \cdot \nabla p = 0, \tag{31}$$

where $\mathbf{u}\cdot\nabla p \sim O(Ma^3)$ and thus it is negligible [37].

The particle distribution function h_α for the composition C is related to f_α by $h_\alpha = (C/\rho) f_\alpha$ and $h_\alpha^{eq} = (C/\rho) f_\alpha^{eq}$ [28]. Taking the total derivative D_t of the new variable h_α gives:

$$\begin{aligned} \frac{\partial h_\alpha}{\partial t} + \mathbf{e}_\alpha \cdot \nabla h_\alpha &= \frac{C}{\rho} \left[-\frac{1}{\lambda}(f_\alpha - f_\alpha^{eq}) + \frac{(\mathbf{e}_\alpha - \mathbf{u})\cdot\mathbf{F}}{c_s^2}\Gamma_\alpha \right] \\ &= -\frac{1}{\lambda}(h_\alpha - h_\alpha^{eq}) + f_\alpha \frac{D}{Dt}\left(\frac{C}{\rho}\right) + \frac{C}{\rho c_s^2}(\mathbf{e}_\alpha - \mathbf{u}) \cdot \left[\nabla \rho c_s^2 - (\nabla p + C\nabla\mu) \right] \Gamma_\alpha. \end{aligned} \tag{32}$$

f_α of the second term on the right-hand side is approximated by $f_\alpha^{eq} = \rho\Gamma_\alpha$, as it is assumed to approximate the intermolecular forcing term in Eq. (23). Furthermore, due to $\nabla\cdot\mathbf{u} = 0$ and Eq. (22):

$$f_\alpha \frac{D}{Dt}\left(\frac{C}{\rho}\right) \approx \left(\frac{\partial C}{\partial t} + \mathbf{e}_\alpha \cdot \nabla C \right) \Gamma_\alpha - \frac{C}{\rho}\left(\frac{\partial \rho}{\partial t} + \mathbf{e}_\alpha \cdot \nabla \rho \right) \Gamma_\alpha = \left[(\mathbf{e}_\alpha - \mathbf{u}) \cdot \nabla C + M\nabla^2 \hat{\mu} \right] \Gamma_\alpha - \frac{C}{\rho}(\mathbf{e}_\alpha - \mathbf{u}) \cdot \nabla \rho \Gamma_\alpha. \tag{33}$$

Finally, Eq. (32) becomes:

$$\frac{\partial h_\alpha}{\partial t} + \mathbf{e}_\alpha \cdot \nabla h_\alpha = -\frac{1}{\lambda}(h_\alpha - h_\alpha^{eq}) + M\nabla^2\hat{\mu}\Gamma_\alpha + (\mathbf{e}_\alpha - \mathbf{u}) \cdot \left[\nabla C - \frac{C}{\rho c_s^2}(\nabla p + C\nabla\mu) \right] \Gamma_\alpha. \tag{34}$$

The Chapman–Enskog expansion is considered to examine Eq. (34) in the long-wavelength and low-frequency limit. The time derivative is expanded as $\partial_t = K\partial_{t_0} + K^2\partial_{t_1} + \cdots$, the space derivative as $\nabla = K\nabla_1$, and the distribution function for the composition as

$$h_\alpha = h_\alpha^{eq} + Kh_\alpha^{(1)} + K^2 h_\alpha^{(2)} + \cdots, \tag{35}$$

with K being the Knudsen number [34]. The first-order Chapman–Enskog approximation of Eq. (34) is

$$\frac{\partial h_\alpha^{eq}}{\partial t_0} + \mathbf{e}_\alpha \cdot \nabla_1 h_\alpha^{eq} = -\frac{h_\alpha^{(1)}}{\lambda} + M\nabla_1^2 \hat{\mu} \Gamma_\alpha + (\mathbf{e}_\alpha - \mathbf{u}) \cdot \left[\nabla_1 C - \frac{C}{\rho c_s^2}(\nabla_1 p + C\nabla_1 \mu)\right] \Gamma_\alpha. \tag{36}$$

The integral of Eq. (36) over velocity space leads to:

$$\frac{\partial C}{\partial t_0} + \nabla_1 \cdot (\mathbf{u}C) = M\nabla_1^2 \hat{\mu}, \tag{37}$$

which is the advective Cahn–Hilliard equation Eq. (22) when $\nabla_1 \cdot \mathbf{u} = 0$. The second-order Chapman-Enskog approximation of Eq. (34) is

$$\frac{\partial h_\alpha^{eq}}{\partial t_1} + \left[\frac{\partial}{\partial t_0} + \mathbf{e}_\alpha \cdot \nabla_1\right] h_\alpha^{(1)} = -\frac{h_\alpha^{(2)}}{\lambda}. \tag{38}$$

Substituting $h_\alpha^{(1)}$ from Eq. (36) into Eq. (38) and integrating Eq. (38) over velocity space gives:

$$\frac{\partial C}{\partial t_1} = 0, \tag{39}$$

which is because the original intermolecular forcing terms in Eq. (23) are retained in both Eqs. (28) and (34).

4. Discretizations

4.1. Spatial gradients

The second-order central difference (CD) approximation of the directional derivative of a variable ϕ along characteristics is obtained at a lattice site ($\mathbf{x}$) from the values of ϕ at neighboring integer lattice sites:

$$\delta t \mathbf{e}_\alpha \cdot \nabla^{CD} \phi|_{(\mathbf{x})} = \frac{1}{2}[\phi(\mathbf{x} + \mathbf{e}_\alpha \delta t) - \phi(\mathbf{x} - \mathbf{e}_\alpha \delta t)], \tag{40}$$

or based on the values of ϕ at half-integer (HI) lattice sites:

$$\delta t \mathbf{e}_\alpha \cdot \nabla^{HI} \phi|_{(\mathbf{x})} = \left[\phi\left(\mathbf{x} + \frac{1}{2}\mathbf{e}_\alpha \delta t\right) - \phi\left(\mathbf{x} - \frac{1}{2}\mathbf{e}_\alpha \delta t\right)\right]. \tag{41}$$

The second derivative of ϕ along characteristics is obtained by applying the directional derivative twice at half-integer lattice sites:

$$(\delta t \mathbf{e}_\alpha \cdot \nabla)^2 \phi|_{(\mathbf{x})} = \delta t \mathbf{e}_\alpha \cdot \nabla^{HI}\left[\delta t \mathbf{e}_\alpha \cdot \nabla^{HI} \phi|_{\left(\mathbf{x} + \frac{1}{2}\mathbf{e}_\alpha \delta t\right)} - \delta t \mathbf{e}_\alpha \cdot \nabla^{HI} \phi|_{\left(\mathbf{x} - \frac{1}{2}\mathbf{e}_\alpha \delta t\right)}\right] = [\phi(\mathbf{x} + \mathbf{e}_\alpha \delta t) - 2\phi(\mathbf{x}) + \phi(\mathbf{x} - \mathbf{e}_\alpha \delta t)]. \tag{42}$$

For discretization of the directional derivative of ϕ at $(\mathbf{x} - \mathbf{e}_\alpha \delta t)$, the biased difference (BD) approximation in the direction of backward characteristics is derived by Taylor-series expanding $\nabla^{CD}\phi$ around the point ($\mathbf{x}$) using the central differences up to second-order in $\delta t\, \mathbf{e}_\alpha$:

$$\delta t \mathbf{e}_\alpha \cdot \nabla^{BD} \phi|_{(\mathbf{x} - \mathbf{e}_\alpha \delta t)} \cong \delta t \mathbf{e}_\alpha \cdot \nabla^{CD} \phi|_{(\mathbf{x})} - (\delta t \mathbf{e}_\alpha \cdot \nabla)^2 \phi|_{(\mathbf{x})} = \frac{1}{2}[-\phi(\mathbf{x} + \mathbf{e}_\alpha \delta t) + 4\phi(\mathbf{x}) - 3\phi(\mathbf{x} - \mathbf{e}_\alpha \delta t)]. \tag{43}$$

When used in conjunction with the central difference at ($\mathbf{x}$), the biased difference approximation at $(\mathbf{x} - \mathbf{e}_\alpha\, \delta t)$ requires the same compact grid support of $(\mathbf{x} + \mathbf{e}_\alpha \delta t, \mathbf{x}, \mathbf{x} - \mathbf{e}_\alpha \delta t)$. Although Eq. (43) is not conservative at $(\mathbf{x} - \mathbf{e}_\alpha \delta t)$, it is conservative at ($\mathbf{x}$), and therefore globally conservative.

Derivatives other than the directional derivatives can be obtained by taking moments of the directional derivatives with appropriate weights to ensure isotropy.

$$\nabla^{BD} \phi|_{(\mathbf{x})} = \frac{1}{c_s^2 \delta t} \sum_{\alpha \neq 0} t_\alpha \mathbf{e}_\alpha \left(\delta t \mathbf{e}_\alpha \cdot \nabla^{BD}\right) \phi|_{(\mathbf{x})}, \tag{44}$$

$$\nabla^{CD} \phi|_{(\mathbf{x})} = \frac{1}{c_s^2 \delta t} \sum_{\alpha \neq 0} t_\alpha \mathbf{e}_\alpha \left(\delta t \mathbf{e}_\alpha \cdot \nabla^{CD}\right) \phi|_{(\mathbf{x})},$$

$$\nabla^2 \phi|_{(\mathbf{x})} = \frac{1}{c_s^2 \delta t^2} \sum_{\alpha \neq 0} t_\alpha (\delta t \mathbf{e}_\alpha \cdot \nabla)^2 \phi|_{(\mathbf{x})}.$$

The second-order mixed difference (*MD*) approximation is an average of the central and biased differences:

$$\delta t\mathbf{e}_\alpha\cdot\nabla^{MD}\phi|_{(\mathbf{x})}=\frac{1}{2}\left[\delta t\mathbf{e}_\alpha\cdot\nabla^{BD}\phi+\delta t\mathbf{e}_\alpha\cdot\nabla^{CD}\phi\right]_{(\mathbf{x})},\tag{45}$$
$$\nabla^{MD}\phi|_{(\mathbf{x})}=\frac{1}{2}\left[\nabla^{BD}\phi+\nabla^{CD}\phi\right]_{(\mathbf{x})}.$$

4.2. Lattice Boltzmann equations

The LBE for Eq. (28) at (**x**,*t*) is obtained by applying the trapezoidal rule along characteristics over time step δt:

$$\begin{aligned}g_\alpha(\mathbf{x},t)=g_\alpha(\mathbf{x}-\mathbf{e}_\alpha\delta t,t-\delta t)&-\frac{g_\alpha-g_\alpha^{eq}}{2\tau}\bigg|_{(\mathbf{x}-\mathbf{e}_\alpha\delta t,t-\delta t)}-\frac{g_\alpha-g_\alpha^{eq}}{2\tau}\bigg|_{(\mathbf{x},t)}+\frac{\delta t}{2}(\mathbf{e}_\alpha-\mathbf{u})\\&\cdot\left[\nabla^{BD}\rho c_s^2(\Gamma_\alpha-\Gamma_\alpha(0))-C\nabla^{BD}\mu\Gamma_\alpha\right]_{(\mathbf{x}-\mathbf{e}_\alpha\delta t,t-\delta t)}+\frac{\delta t}{2}(\mathbf{e}_\alpha-\mathbf{u})\cdot\left[\nabla^{CD}\rho c_s^2(\Gamma_\alpha-\Gamma_\alpha(0))-C\nabla^{CD}\mu\Gamma_\alpha\right]_{(\mathbf{x},t)},\end{aligned}\tag{46}$$

where the nondimensional relaxation time $\tau=\lambda/\delta t$ is related to the kinematic viscosity by $\nu=\tau c_s^2\delta t$. Eq. (46) is recast in a simpler form:

$$\begin{aligned}\bar g_\alpha(\mathbf{x},t)=\bar g_\alpha(\mathbf{x}-\mathbf{e}_\alpha\delta t,t-\delta t)&-\frac{1}{\tau+1/2}\left(\bar g_\alpha-\bar g_\alpha^{eq}\right)\Big|_{(\mathbf{x}-\mathbf{e}_\alpha\delta t,t-\delta t)}\\&+\delta t(\mathbf{e}_\alpha-\mathbf{u})\cdot\left[\nabla^{MD}\rho c_s^2(\Gamma_\alpha-\Gamma_\alpha(0))-C\nabla^{MD}\mu\Gamma_\alpha\right]_{(\mathbf{x}-\mathbf{e}_\alpha\delta t,t-\delta t)},\end{aligned}\tag{47}$$

where $\bar g_\alpha$ and $\bar g_\alpha^{eq}$ are the modified particle and equilibrium distribution functions, respectively, which are defined as

$$\bar g_\alpha=g_\alpha+\frac{1}{2\tau}\left(g_\alpha-g_\alpha^{eq}\right)-\frac{\delta t}{2}(\mathbf{e}_\alpha-\mathbf{u})\cdot\left[\nabla^{CD}\rho c_s^2(\Gamma_\alpha-\Gamma_\alpha(0))-C\nabla^{CD}\mu\Gamma_\alpha\right],\tag{48}$$

$$\bar g_\alpha^{eq}=g_\alpha^{eq}-\frac{\delta t}{2}(\mathbf{e}_\alpha-\mathbf{u})\cdot\left[\nabla^{CD}\rho c_s^2(\Gamma_\alpha-\Gamma_\alpha(0))-C\nabla^{CD}\mu\Gamma_\alpha\right].\tag{49}$$

The LBE for Eq. (34) at (**x**, *t*) is derived similarly to Eq. (46):

$$\begin{aligned}h_\alpha(\mathbf{x},t)=h_\alpha(\mathbf{x}-\mathbf{e}_\alpha\delta t,t-\delta t)&-\frac{h_\alpha-h_\alpha^{eq}}{2\tau}\bigg|_{(\mathbf{x}-\mathbf{e}_\alpha\delta t,t-\delta t)}-\frac{h_\alpha-h_\alpha^{eq}}{2\tau}\bigg|_{(\mathbf{x},t)}+\frac{\delta t}{2}M\nabla^2\hat\mu\Gamma_\alpha\Big|_{(\mathbf{x}-\mathbf{e}_\alpha\delta t,t-\delta t)}+\frac{\delta t}{2}M\nabla^2\hat\mu\Gamma_\alpha\Big|_{(\mathbf{x},t-\delta t)}\\&+\frac{\delta t}{2}(\mathbf{e}_\alpha-\mathbf{u})\cdot\left[\nabla^{BD}C-\frac{C}{\rho c_s^2}\left(\nabla^{BD}p+C\nabla^{BD}\mu\right)\right]\Gamma_\alpha\Big|_{(\mathbf{x}-\mathbf{e}_\alpha\delta t,t-\delta t)}\\&+\frac{\delta t}{2}(\mathbf{e}_\alpha-\mathbf{u})\cdot\left[\nabla^{CD}C-\frac{C}{\rho c_s^2}\left(\nabla^{CD}p+C\nabla^{CD}\mu\right)\right]\Gamma_\alpha\Big|_{(\mathbf{x},t)}.\end{aligned}\tag{50}$$

Notice that $M\nabla^2\hat\mu\Gamma_\alpha|_{(\mathbf{x},t)}$ is approximated by $M\nabla^2\hat\mu\Gamma_\alpha|_{(\mathbf{x},t-\delta t)}$ in order to avoid implicitness in *C*. This approximation still remains accurate to second-order. The modified distribution functions $\bar h_\alpha$ and $\bar h_\alpha^{eq}$ are defined as

$$\bar h_\alpha=h_\alpha+\frac{1}{2\tau}\left(h_\alpha-h_\alpha^{eq}\right)-\frac{\delta t}{2}(\mathbf{e}_\alpha-\mathbf{u})\cdot\left[\nabla^{CD}C-\frac{C}{\rho c_s^2}\left(\nabla^{CD}p+C\nabla^{CD}\mu\right)\right]\Gamma_\alpha,\tag{51}$$

$$\bar h_\alpha^{eq}=h_\alpha^{eq}-\frac{\delta t}{2}(\mathbf{e}_\alpha-\mathbf{u})\cdot\left[\nabla^{CD}C-\frac{C}{\rho c_s^2}\left(\nabla^{CD}p+C\nabla^{CD}\mu\right)\right]\Gamma_\alpha.\tag{52}$$

The LBE for Eq. (50) then becomes:

$$\begin{aligned}\bar h_\alpha(\mathbf{x},t)=\bar h_\alpha(\mathbf{x}-\mathbf{e}_\alpha\delta t,t-\delta t)&-\frac{1}{\tau+1/2}\left(\bar h_\alpha-\bar h_\alpha^{eq}\right)\Big|_{(\mathbf{x}-\mathbf{e}_\alpha\delta t,t-\delta t)}+\frac{\delta t}{2}M\nabla^2\hat\mu\Gamma_\alpha\Big|_{(\mathbf{x}-\mathbf{e}_\alpha\delta t,t-\delta t)}+\frac{\delta t}{2}M\nabla^2\hat\mu\Gamma_\alpha\Big|_{(\mathbf{x},t-\delta t)}\\&+\delta t(\mathbf{e}_\alpha-\mathbf{u})\cdot\left[\nabla^{MD}C-\frac{C}{\rho c_s^2}\left(\nabla^{MD}p+C\nabla^{MD}\mu\right)\right]\Gamma_\alpha\Big|_{(\mathbf{x}-\mathbf{e}_\alpha\delta t,t-\delta t)}.\end{aligned}\tag{53}$$

We choose $\tau=1/2$ in the above equation, because the recovered Cahn–Hilliard equation is not affected by the choice of τ as shown in Eqs. (36) and (38). The composition, dynamic pressure, and momentum can be computed by taking the zeroth and first moments of the modified particle distribution functions:

$$C = \sum_\alpha \bar{h}_\alpha, \tag{54}$$

$$\rho \mathbf{u} = \frac{1}{c_s^2} \sum_\alpha \mathbf{e}_\alpha \bar{g}_\alpha - \frac{\delta t}{2} C \nabla^{CD} \mu, \tag{55}$$

$$p = \sum_\alpha \bar{g}_\alpha + \frac{\delta t}{2} \mathbf{u} \cdot \nabla^{CD} \rho c_s^2. \tag{56}$$

The dimensionless relaxation time is taken as an inverse function of the composition:

$$\frac{1}{\tau} = \frac{C}{\tau_1} + \frac{1-C}{\tau_2}, \tag{57}$$

which implies that the collision frequency is linearly proportional to C.

4.3. Boundary conditions

Unknown particle distribution functions at the wall nodes are obtained from the bounce-back scheme, in which the outgoing particle distribution function f_α reflects back at the wall boundary and continues streaming as if the reflected particle distribution function $f_{\bar{\alpha}}$ is a continuation of f_α in the opposite direction as illustrated in Fig. 2(a). Here, $\mathbf{e}_{\bar{\alpha}} \cdot \mathbf{n} > 0$ and $\mathbf{e}_\alpha \cdot \mathbf{n} < 0$ and at the wall boundary node ($\mathbf{x}_s$), $f_{\bar{\alpha}}(\mathbf{x}_s) = f_\alpha(\mathbf{x}_s)$, which is followed by immediate relaxation toward the equilibrium state with the density and velocity at the solid surface [26]. As is illustrated in Fig. 2(b), the bounce-back scheme can alternatively be interpreted as the particle distribution function $f_{\bar{\alpha}}$ traveling continuously from the solid nodes, if the unknown profile of $f_{\bar{\alpha}}$ in the solid nodes is taken as the mirror image of f_α in the fluid nodes. This alternative interpretation is not used to compute the particle distribution functions in the present study, but could be useful when the finite difference approximation of the directional derivative is required.

In Fig. 3(a) a certain profile of a macroscopic variable ϕ is assumed in the fluid domain. Evaluation of the first and second derivatives of ϕ at the boundary node ($\mathbf{x}_s$) and neighboring nodes ($\mathbf{x}_s - \mathbf{e}_\alpha \delta t$) typically requires information at ($\mathbf{x}_s + \mathbf{e}_\alpha \delta t$) and/or ($\mathbf{x}_s + 2\mathbf{e}_\alpha \delta t$). Note that Eqs. (10) and (20) are the boundary conditions for $\nabla^2 \mu$ and $\nabla^2 C$, and valid only at equilibrium, and thus should not be imposed for the terms unrelated to the free energy. A one-sided difference may be considered, but it may introduce unphysical mass and momentum fluxes across the wall boundary. Since the macroscopic variables, such as C and p, are calculated from the zeroth moment of the particle distribution functions, the profile of ϕ in the solid is assumed to take the mirror image of ϕ in the fluid as the particle distribution functions do. As shown in Fig. 3(b), when the points ($\mathbf{x}_s + \mathbf{e}_\alpha \delta t$) and ($\mathbf{x}_s + 2\mathbf{e}_\alpha \delta t$) are located outside the computational domain while ($\mathbf{x}_s - \mathbf{e}_\alpha \delta t$) and ($\mathbf{x}_s - 2\mathbf{e}_\alpha \delta t$) are not, any unknown variable ϕ outside the fluid domain is approximated by

$$\begin{aligned} \phi(\mathbf{x}_s + \mathbf{e}_\alpha \delta t) &= \phi(\mathbf{x}_s - \mathbf{e}_\alpha \delta t), \\ \phi(\mathbf{x}_s + 2\mathbf{e}_\alpha \delta t) &= \phi(\mathbf{x}_s - 2\mathbf{e}_\alpha \delta t). \end{aligned} \tag{58}$$

Eq. (58) imposes no flux condition, $\mathbf{e}_\alpha \cdot \nabla \phi|_s = 0$, and prevents unphysical mass and momentum transfer through the boundary nodes.

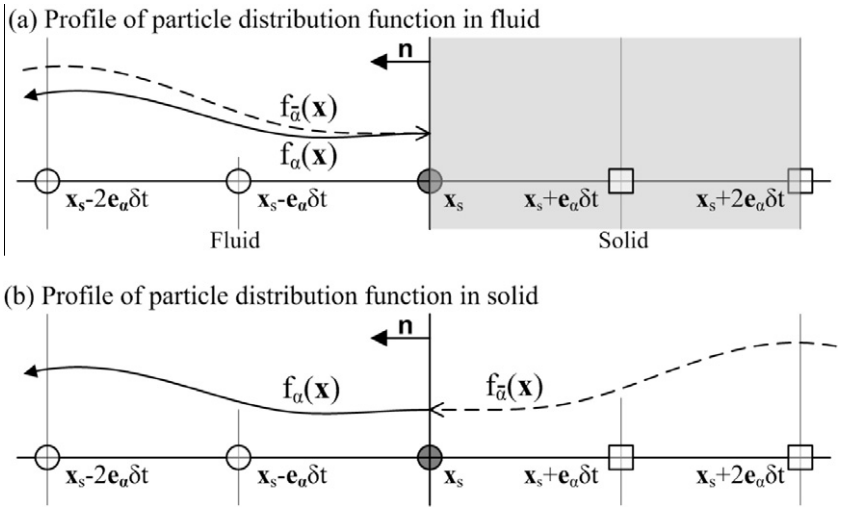

Fig. 2. A schematic illustration of the bounce-back scheme: (a) f_α is an outgoing particle distribution function from the fluid nodes (denoted by circles), which is reflected back at a wall boundary node $\mathbf{x}_s$ to become $f_{\bar{\alpha}}$. (b) Alternatively, $f_{\bar{\alpha}}$ travels continuously from the imaginary solid nodes (denoted by rectangles), if the profile of $f_{\bar{\alpha}}$ in the solid nodes is taken as the mirror image of f_α in the fluid nodes.

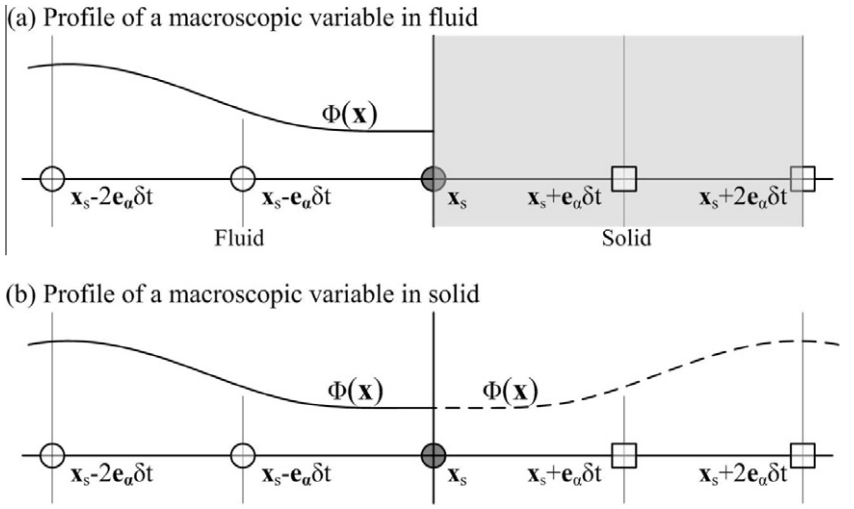

Fig. 3. Profile of an unknown macroscopic variable in the solid taken as a mirror image in the fluid.

The directional derivatives, Eqs. (41) and (43), in the outgoing direction $\mathbf{e}_\alpha$ are then:

$$\delta t \mathbf{e}_\alpha \cdot \nabla^{CD}\phi|_{(\mathbf{x})} = 0, \tag{59}$$

$$\delta t \mathbf{e}_\alpha \cdot \nabla^{BD}\phi|_{(\mathbf{x}_s)} = \frac{1}{2}[-\phi(\mathbf{x}_s - 2\mathbf{e}_\alpha\delta t) + 4\phi(\mathbf{x}_s - \mathbf{e}_\alpha\delta t) - 3\phi(\mathbf{x}_s)],$$

$$\delta t \mathbf{e}_\alpha \cdot \nabla^{BD}\phi|_{(\mathbf{x}_s - \mathbf{e}_\alpha\delta t)} = \frac{1}{2}[4\phi(\mathbf{x}_s) - 4\phi(\mathbf{x}_s - \mathbf{e}_\alpha\delta t)].$$

The directional derivatives in the incoming direction $\mathbf{e}_{\bar{\alpha}}$ are:

$$\delta t \mathbf{e}_{\bar{\alpha}} \cdot \nabla^{CD}\phi|_{(\mathbf{x}_s)} = 0, \tag{60}$$

$$\delta t \mathbf{e}_{\bar{\alpha}} \cdot \nabla^{BD}\phi|_{(\mathbf{x}_s)} = \frac{1}{2}[-\phi(\mathbf{x}_s + 2\mathbf{e}_{\bar{\alpha}}\delta t) + 4\phi(\mathbf{x}_s + \mathbf{e}_{\bar{\alpha}}\delta t) - 3\phi(\mathbf{x}_s)].$$

Likewise, the second derivative, Eq. (42), becomes:

$$\left(\delta t \mathbf{e}_\alpha \cdot \nabla^{C}\right)^2 \phi|_{(\mathbf{x}_s)} = -[2\phi(\mathbf{x}_s) - 2\phi(\mathbf{x}_s - \mathbf{e}_\alpha\delta t)]. \tag{61}$$

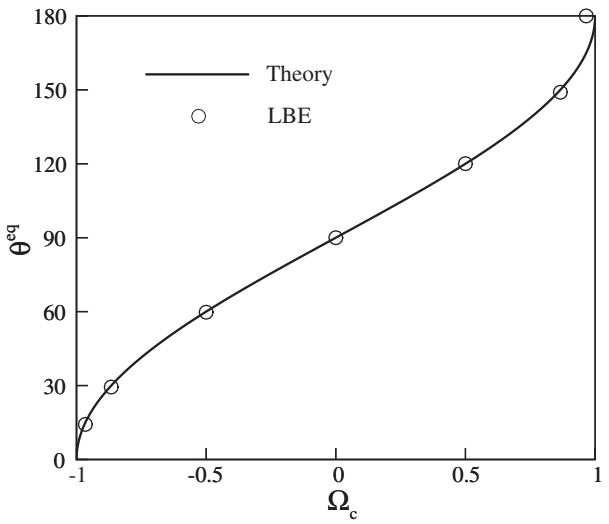

Fig. 4. The equilibrium contact angle θ^{eq} vs. dimensionless wetting potential Ω_c.

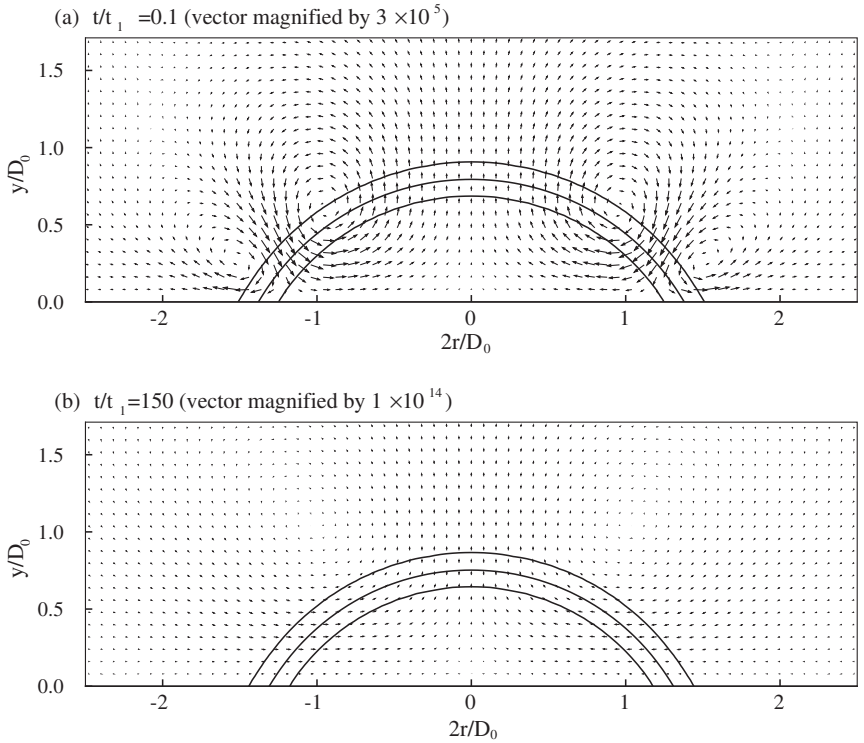

Fig. 5. Velocity fields around a drop on a surface with $\theta^{eq} = 60°$. Vectors are magnified by (a) 3×10^5 at $t/t_2 = 0.1$ and (b) 1×10^{14} at $t/t_2 = 150$. Three contour levels represent $C = 0.1$, 0.5, and 0.9.

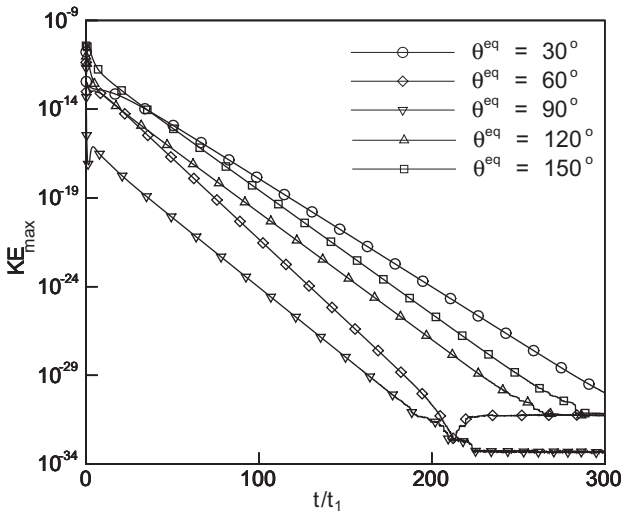

Fig. 6. Time evolution of the maximum kinetic energy per unit volume with different values of θ^{eq} at $\xi = 5$, $R_{90°} = 25$, $\rho_1 = 1.0$, and $\rho_2 = 1.188 \times 10^{-3}$. Time is normalized to the viscous time scale of the liquid phase $t_1 = \rho_1 v_1 R_{\theta^{eq}}/\sigma$. τ and σ are fixed at 0.2 and 1×10^{-4}, respectively.

The directional derivatives in the incoming direction $\mathbf{e}_{\tilde{\alpha}}$ can be found in the same manner. Derivatives other than the directional derivatives can be obtained by taking moments of the directional derivatives.

5. Numerical test

5.1. Equilibrium drop on homogeneous surfaces

A two dimensional liquid drop on a solid surface with equilibrium contact angles ranging from 15° to 165° is generated at the bottom center of a 200 × 100 computational domain for a D2Q9 lattice [36]. The initial area of the drop with different

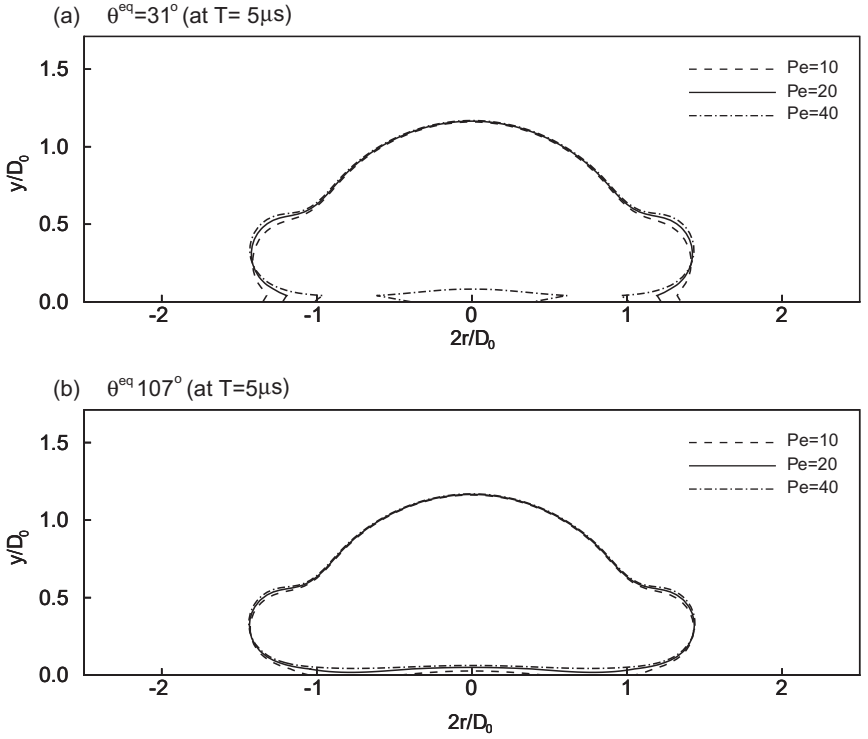

Fig. 7. Cross-sectional images of a 48.8 μm size water drop impacting on dry surfaces of (a) $\theta_{eq} = 31°$ and (b) $\theta_{eq} = 107°$ at 5 μs. The liquid–gas interface is represented by a contour level $C = 0.5$.

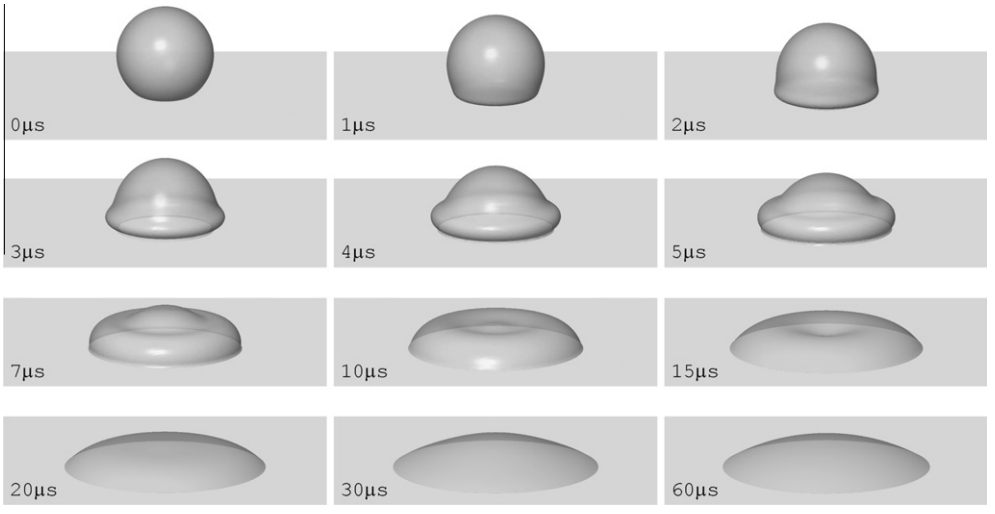

Fig. 8. Time sequence of 48.8 μm size water drop impact on a dry surface of $\theta_{eq} = 31°$. *We* = 12.8 and *Re* = 241.

contact angles is kept constant such that its radius on a neutrally wetting surface is $R_{90^\circ} = 25$ in lattice unit. We fix $\rho_1 = 1.0$, and $\rho_2 = 0.1$, in which case the interface tension is $\sigma = 1 \times 10^{-4}$. The interface thickness, relaxation time, and mobility are $\xi = 5$, $\tau = 0.5$, and $M = 0.02/\beta$, respectively. Fig. 4 shows the equilibrium contact angle θ^{eq} as a function of the dimensionless wetting potential Ω for the cubic boundary condition. The equilibrium contact angle is calculated from the measured height and base diameter of a drop on a solid surface at equilibrium. It is assumed that the system reaches equilibrium when the maximum kinetic energy per unit volume drops to zero and the parasitic currents completely disappear. The LBE simulations are compared with the analytic solution, Eq. (19), and the variation of the simulated contact angle from theory is less than 1° for $\theta^{eq} \leqslant 150^\circ$. The LBE results start to deviate from Eq. (19) for $\theta^{eq} > 150^\circ$, which is attributed to the fact that since the area of the drop is fixed in all simulations, the radius of the drop is smaller for non-wetting surfaces and the grid resolution to represent a drop deteriorates as a result.

Fig. 5(a) is a velocity vector field magnified by 3×10^5 at dimensionless time $t/t_1 = 0.1$, where $t_1 = \rho_1 v_1 R_{\theta^{eq}}/\sigma$ is the viscous time of the liquid phase (fluid 1). Fig. 5(a) clearly indicates the presence of organized eddies around the phase interface

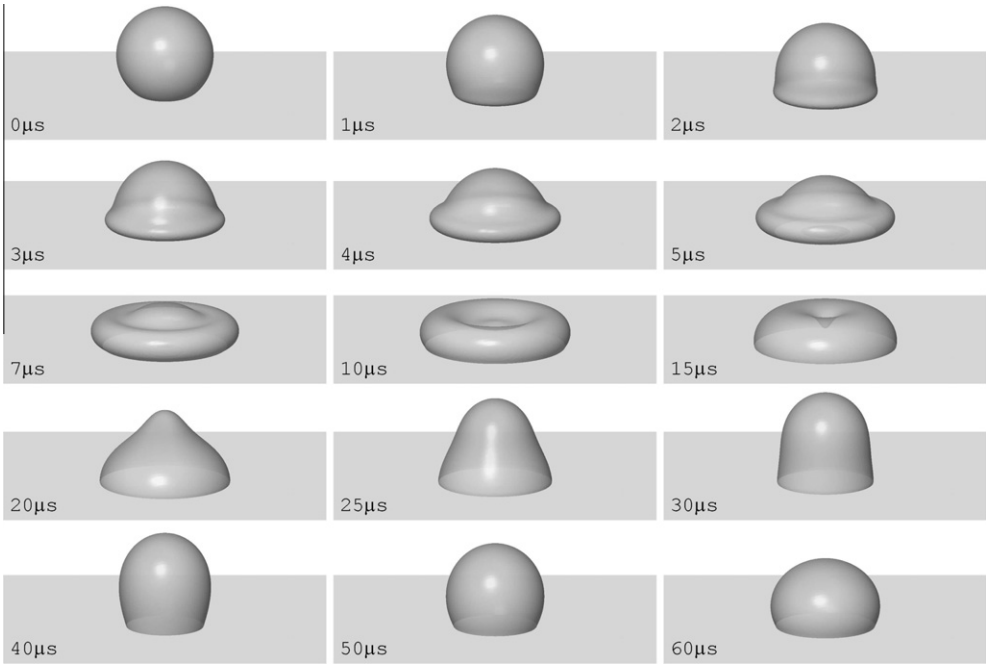

Fig. 9. Time sequence of 48.8 μm size water drop impact on a dry surface of $\theta_{eq} = 107^\circ$. $We = 12.8$ and $Re = 241$.

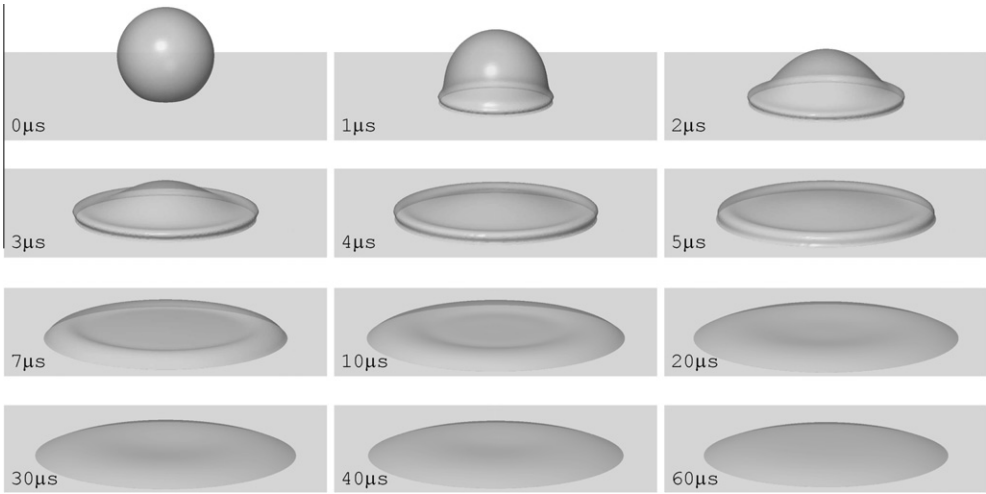

Fig. 10. Time sequence of 50.5 μm size water drop impact on a dry surface of $\theta_{eq} = 31^\circ$. $We = 103$ and $Re = 685$.

and contact line. This is due to the imbalance between the dynamic pressure gradient and the chemical potential gradient, which has not reached the equilibrium state yet. At $t/t_1 = 150$, the organized eddies disappear and the parasitic currents are eliminated to round-off as shown in Fig. 5(b). Unlike the LBE simulation with the linear boundary condition [26], enrichment (or depletion) of the liquid phase in contact with a solid surface is not observed, because the cubic boundary condition takes only the interactions between the liquid–gas phase interface and the solid into account.

Time evolution of the maximum kinetic energy per unit volume with different contact angles is shown in Fig. 6, where the time is normalized to t_1. In the simulations, $\rho_1 = 1.0$ and $\rho_2 = 1.188 \times 10^{-3}$ are used. The interface tension, interface thick-

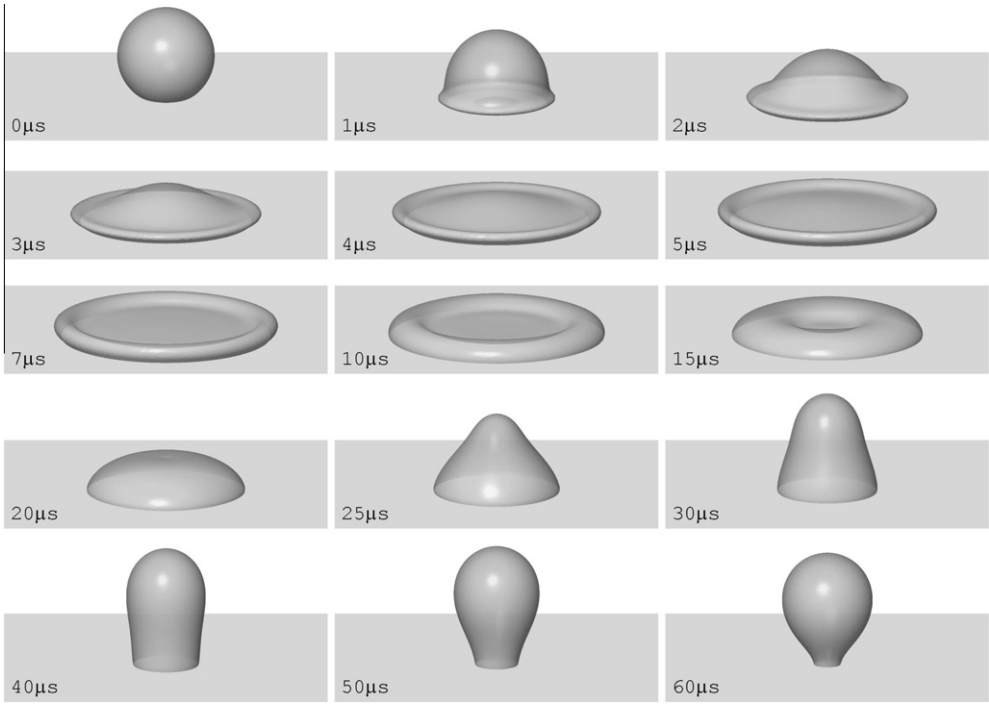

Fig. 11. Time sequence of 50.5 μm size water drop impact on a dry surface of $\theta_{eq} = 107°$. $We = 103$ and $Re = 685$.

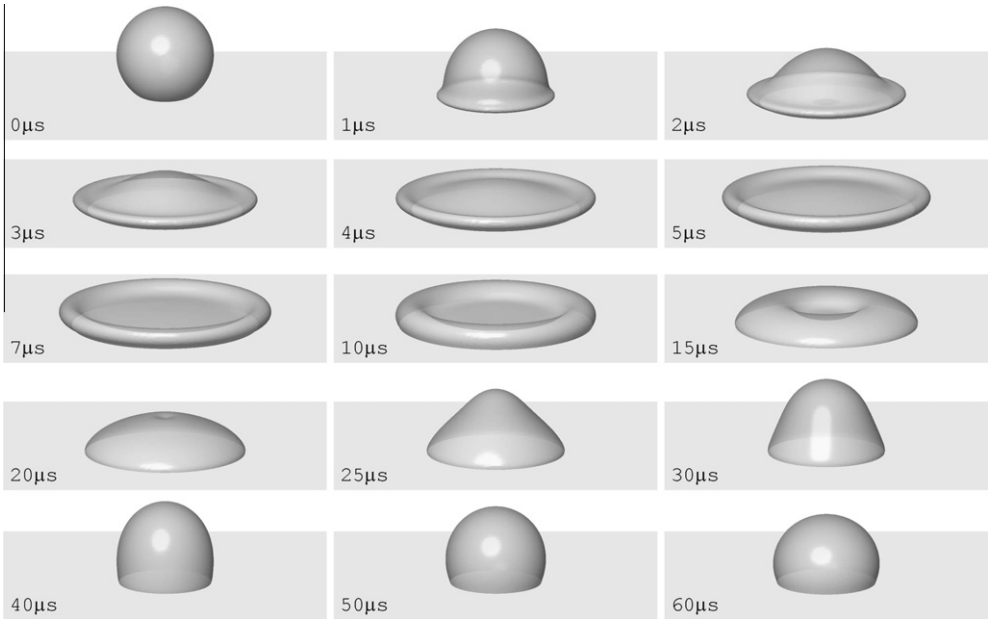

Fig. 12. Same as Fig. 11 but with the linear relaxation time from Eq. (62).

ness, relaxation time, and mobility are $\sigma = 1 \times 10^{-4}$, $\xi = 5$, $\tau = 0.2$, and $M = 0.02/\beta$, respectively. Although some irregularities in the convergence history are apparent, overall convergence rates for different θ^{eq} are similar, except for $\theta^{eq} = 30^{\circ}$. As noted in [26], the liquid–gas interface at small θ^{eq} is too close to the solid surface making it difficult for the liquid at the solid surface to reach the elevated equilibrium density due to inclusion of curvature. Moreover, the presence of the dynamic pressure p in Eq. (28) affects the balance in the chemical potential gradient. Since the role of p is to enforce the incompressibility, it is not to be recast or absorbed into the chemical potential through thermodynamic identity. There is a possibility that the dynamic pressure gradient may not be balanced by the interfacial tension when the system is away from the equilibrium state. However, as the free energy is minimized through Cahn–Hilliard diffusion, the dynamic pressure gradient is gradually decoupled from the chemical potential gradient, and at equilibrium, the dynamic pressure gradient becomes zero everywhere, eliminating the parasitic currents. Finally, the fixed interfacial tension at $\sigma = 1 \times 10^{-4}$ for different radii of curvature changes the pressure difference across the drop interface. As M increases, faster convergence toward the equilibrium state is achieved [28].

5.2. Drop impact on dry surfaces

In this section, we consider micron-scale water drop impact on dry surfaces. Understanding of the drop impaction process requires knowledge about the fluid flow within the drop and the surrounding gas, and about the movement of the dynamic contact line [38]. Immediately after the impact, the cross-section of the drop resembles a truncated sphere, but as the liquid continues to move radially, a nearly flat layer or blob is formed. The entire spreading stage lasts $O(10)$ μs and the drop begins

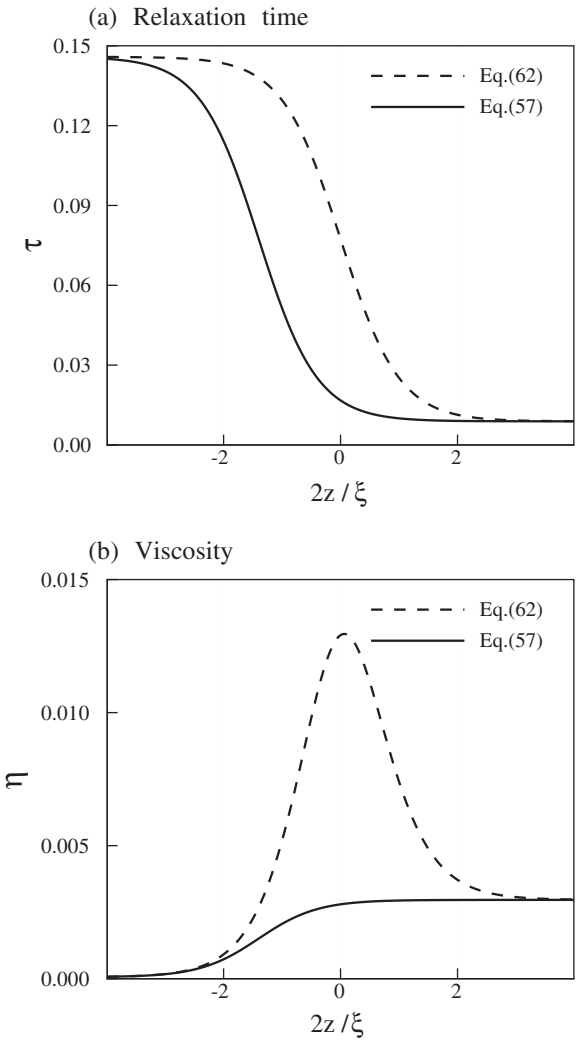

Fig. 13. Profiles of (a) relaxation time τ and (b) dynamic viscosity η computed by Eqs. (57) and (62).

to retract due to interfacial tension afterwards [29]. The extent and speed of retraction depend on the impact velocity and the wettability of the solid substrate. The liquid-substrate interaction at the contact line becomes increasingly important toward the end of drop spreading when inertial forces become small [39]. In general, retraction is weaker as the contact angle decreases.

A three dimensional water droplet is generated at the corner of a $100 \times 100 \times 100$ computational domain for a D3Q27 lattice [36]. The boundaries are all symmetric except at the solid surface, where the wall boundary condition developed in the previous section is imposed. The interface thickness and initial drop radius are $\xi = 5$ and $R_0 = 25$, respectively. Computations are performed at two contact angles of 31° and 107°. The impaction process is primarily described by two independent dimensionless numbers in addition to the contact angle, namely the Weber number (We), and Ohnesorge number (Oh) or Reynolds number (Re). These dimensionless numbers are defined as follows:

$$We = \frac{\rho_1 U_0^2 D_0}{\sigma};$$

$$Oh = \frac{\eta_1}{\sqrt{\rho_1 \sigma D_0}} \quad \text{or} \quad Re = \frac{\sqrt{We}}{Oh},$$

where U_0 is the drop impact speed, D_0 is the diameter of the spherical drop prior to impact, η_1 is the liquid viscosity. Following [29], we consider $Oh \sim 0.015$, and two Weber numbers of 13 and 103 for a fixed density ratio of 842 (*i.e.*, $\rho_1 = 1.0$ and $\rho_2 = 1.188 \times 10^{-3}$), and a viscosity ratio of 51. The coefficient for E_A is $\beta_A = 0.25$.

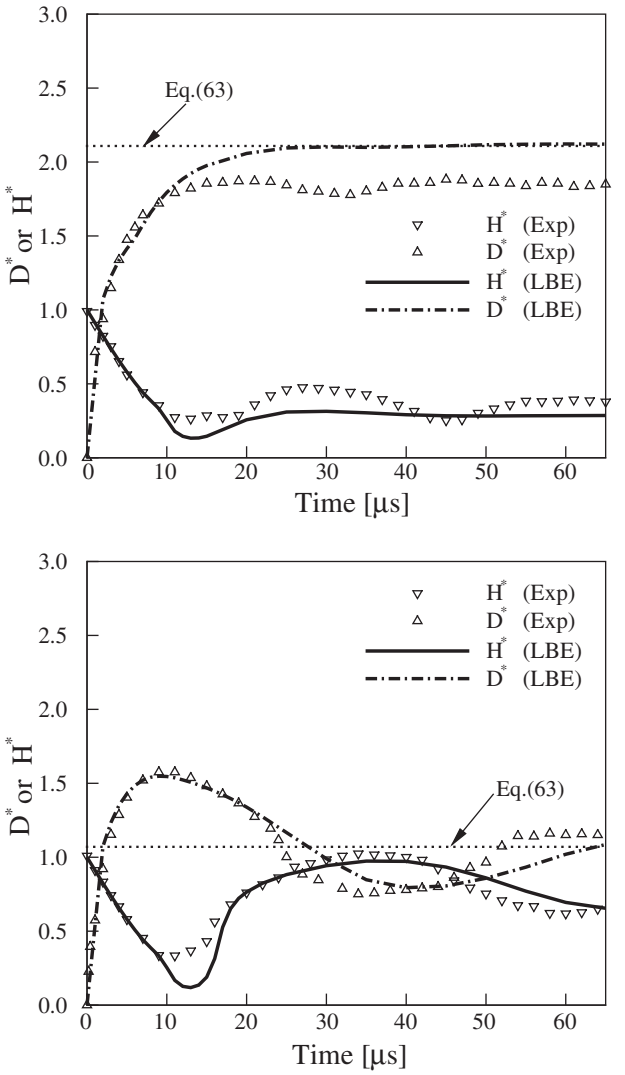

Fig. 14. Variation of the spreading ratio D^* and dimensionless drop height H^* with time at $D_0 = 48.8$ μm and $We = 12.8$: (a) $\theta^{eq} = 31°$; (b) $\theta^{eq} = 107°$.

The effect of the mobility is examined for three different Peclet numbers defined as $Pe = (U_0\kappa^{\frac{1}{2}})/(M\beta^{\frac{3}{2}})$. In Fig. 7, the snapshots of a water drop impacting on solid substrates with $\theta^{eq} = 31^\circ$ and $\theta^{eq} = 107^\circ$ are shown at 5 μs after impact. The liquid–gas interface is represented by a contour level $C = 0.5$. The size of a real drop is $D_0 = 48.8$ μm and the impact speed is $U_0 = 4.36$ m/s, which corresponds to $We = 12.8$ and $Re = 241$. In lattice unit, the impact velocity is $U_{0,LBE} = 0.02$. As Pe decreases, the contact line tends to spread faster because the total energy is minimized through stronger bulk diffusion. This tendency is more pronounced on a wetting surface (Fig. 7(a)), as the stronger bulk diffusion tries to eliminate the inflection point in the liquid–gas interface close to the contact line. In the following simulations, Pe is fixed at 10.

Sequential images of the same water drop impact on a solid substrate with $\theta^{eq} = 31^\circ$ are shown in Fig. 8. As shown in the figure, the initial impact phase is followed by a rapid radial flow where the layer or blob of fluid is formed near the contact line. The contact line lags behind the blob, but after the blob reaches its maximum diameter at around 7 μs, the contact line starts to catch up with the blob and expands slowly outward. Notice that the drop oscillates in the vertical direction between 10 and 20 μs before it reaches its equilibrium shape.

Fig. 9 shows sequential images of the same drop impact on a solid substrate with $\theta^{eq} = 107^\circ$. Unlike impaction on the low-contact angle surface, fluid is accumulated at the leading edge of the blob as the drop spreads and it starts pulling back after the drop reaches its maximum diameter. As the kinetic energy of the drop is converted into surface energy, the drop retracts under the influence of interfacial tension. The drop reaches its maximum spreading before 10 μs. Compared with the $\theta^{eq} = 31^\circ$ case, the shape and height at the center undergo significant changes as the drop retracts. The drop continues to rise to its maximum height at around 30 μs, pauses and spreads again toward the equilibrium shape.

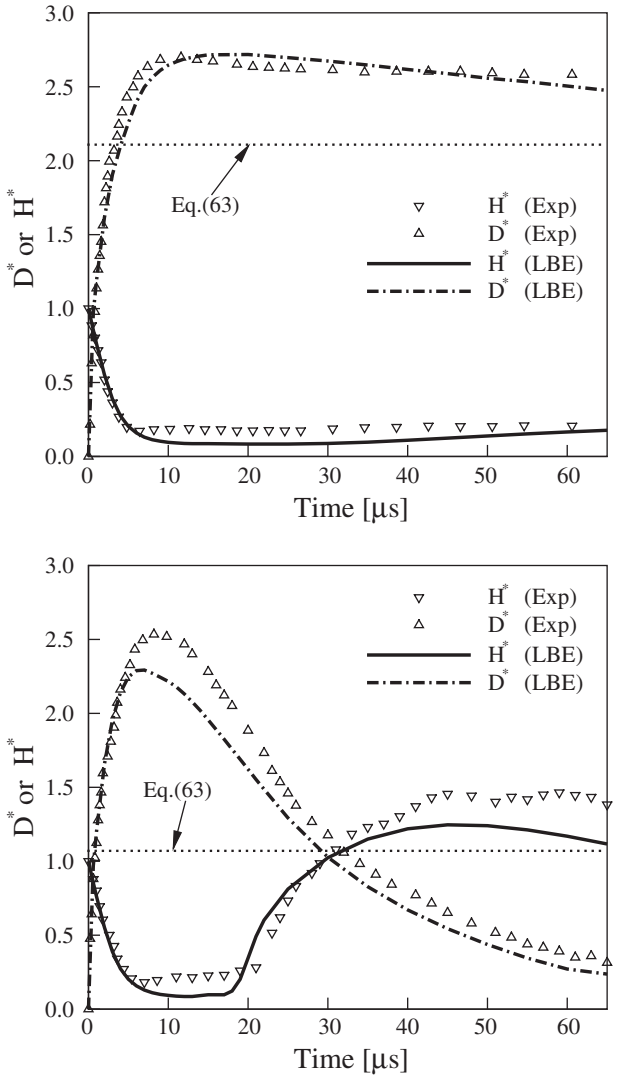

Fig. 15. Variation of spreading ratio D^* and dimensionless drop height H^* with time at $D_0 = 50.5$ μm and $We = 103$: (a) $\theta^{eq} = 31^\circ$; (b) $\theta^{eq} = 107^\circ$.

Sequences of drop impact at higher *We* are presented in Figs. 10 and 11. The size of a real drop is $D_0 = 50.5$ μm and the impact speed is $U_0 = 12.2$ m/s, in which case $We = 103$ and $Re = 685$. In lattice unit, the impact velocity is now $U_{0,LBE} = 0.04$. As the relative magnitude of kinetic and surface energies is *We*, the drop spreads faster for higher *We* and the layer or blob becomes thinner when compared at equal diameter. In addition, the varied surface energy of the substrate indicated by the contact angle has an insignificant influence on the layer thickness, while during spreading, the layer thickness increases. In both cases, the maximum area wetted by the drop is larger than that on a smaller contact angle surface. Also noticeable is that in the first stage of impact, the upper part of the droplet remains undisturbed, which illustrates that for high-speed impacts, the time scale for spreading R_0/U_0 becomes considerably smaller than the time scale for deformation of the drop by interfacial tension $\sqrt{\rho_1 R_0^3/\sigma}$ [38].

On the surface with $\theta^{eq} = 31^\circ$, shown in Fig. 10, the drop retracts very slowly until it reaches the equilibrium shape after maximum spreading. The height of the drop also increases during recoil. Compared with the low impact velocity case, the diameter is larger at a given time with a higher *We*. With $\theta^{eq} = 107^\circ$, shown in Fig. 11, the accumulation of fluid at the leading edge of the blob as the drop spreads is clearly visible and the blob has a larger radius than the contact line during the entire process of spreading, even after maximum spreading is reached. The blob becomes thicker as the drop begins to retract. Eventually, the drop almost rebounds, but fails to lift off from the solid surface. In the experiment by [29], a partial rebound was reported.

If dimensionless relaxation time is determined by a linear function of the composition [6]:

$$\tau = C\tau_1 + (1 - C)\tau_2, \tag{62}$$

rather than Eq. (57), the drop exhibits slower spreading and retraction as shown in Fig. 12. Both the maximum spreading and height after retraction are noticeably reduced. Unlike the drop in Fig. 11 that almost rebounds, the drop in Fig. 12 does not show any sign of rebound and a significant portion of the liquid is always in contact with the solid substrate. The retardation of interface motion is caused by the non-monotonic variation of dynamic viscosity η calculated from Eq. (62). Fig. 13 compares the profiles of the relaxation time τ and the kinetic viscosity η across the planar interface. τ in Eq. (62) is symmetric around $z = 0$ while τ in Eq. (57) is shifted toward the gas phase, both of which share monotonic variation across the interface. However, η obtained from Eq. (62) shows a peak in the interface region with a magnitude several times larger than the bulk viscosities.

Time evolution of the dimensionless diameter or spreading ratio $D^* = D/D_0$ and dimensionless height $H^* = H/D_0$ is shown in Figs. 14 and 15 for $We = 12.8$ and $We = 103$, respectively. In measuring the diameter of a spreading drop, the diameter of the blob is chosen as D when the drop spreads and the diameter of the wetted area is chosen as D when the drop retracts, as illustrated in Fig. 16. During the spreading stage, the diameter of the blob is usually larger than the diameter of the wetted. As recoil begins, the blob disappears.

The agreement of the LBE simulations with experiment [29] is good, particularly at the early times up to <5 μs for both the $We = 12.8$ and $We = 103$ cases. In Fig. 14(a) the experimental results show that the drop reaches an equilibrium state soon after 10 μs, while the LBE result predicts a continued variation of D^* and H^* up to 25 μs. The difference in the final values of D^* between the experiment and simulation is noticeable. D^* at equilibrium with a given contact angle can be found when volume conservation and a spherical cap is assumed [38]:

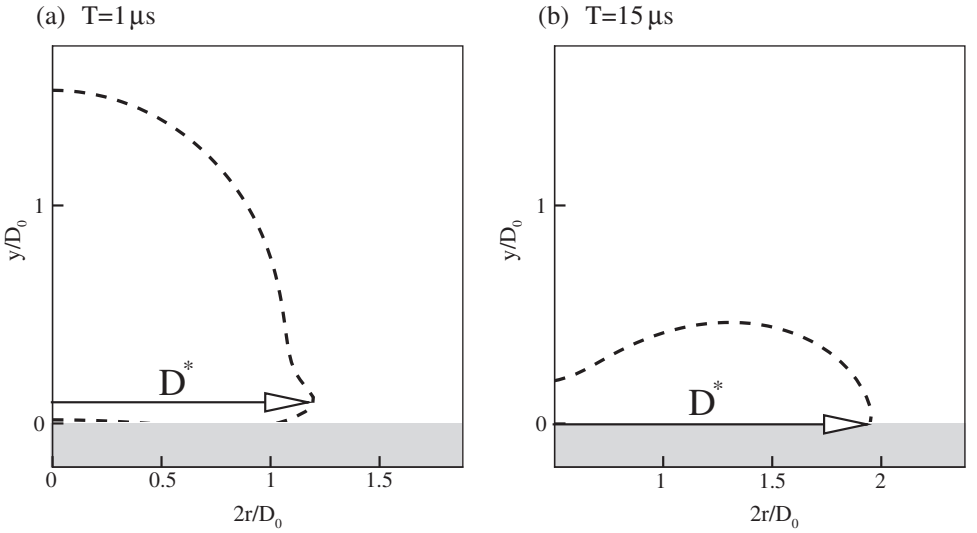

Fig. 16. Definition of the spreading factor D^*: (a) when the drop spreads, the blob diameter is used; (b) when it recoils, the diameter of the wetted area is used.

$$D^* = \left(\frac{8}{\tan\left(\frac{\theta_{eq}}{2}\right)\left(3 + \tan^2\left(\frac{\theta_{eq}}{2}\right)\right)} \right)^{1/3}, \tag{63}$$

which is plotted with a horizontal dotted line in Figs. 14 and 15. It is speculated that the contact line of the real drop is slowed down during retraction and pinned before it achieves the equilibrium contact angle. For the $\theta^{eq} = 107^\circ$ case in Fig. 14(b), both the experiment and the LBE simulation converge to the expected spreading ratio given in Eq. (63) after the drop undergoes some oscillations during retraction.

The influence of *We* emerges in the later stages of spreading, probably because viscous or interfacial tension effects become important later with a larger *We*. As a result, the final radius becomes larger with a larger *We* as shown in Fig. 15. It is also observed that the final spreading ratios are different for small and large contact angles, which confirms that the interfacial tension becomes important in the later stages of drop impact.

6. Concluding remarks

In this study, wall boundary conditions of the LBE method for incompressible binary fluids are proposed and described in detail for the particle distribution function and the forcing terms. They are derived based on the minimization of the free energy subject to polynomial wall free energy and the bounce-back rule. The LBE method is capable of eliminating the parasitic currents to machine accuracy in the presence of a wall boundary. The proposed boundary conditions are capable of reproducing the theoretical values of the contact angles for moderate equilibrium contact angles, but become less accurate for very high contact angles. The LBE method is applied to investigate micron-scale drop (approximately 50 μm in diameter) impact dynamics on solid surfaces with two equilibrium contact angles $\theta^{eq} = 31^\circ$ and 107°. The numerical results are compared with the experimental results and they are in good agreement, particularly at early times after impact. Contact line pinning in the experiment and the finite interface thickness effect in the LBE simulation could contribute to the small discrepancies found in the comparison.

Acknowledgments

This work was supported by the National Science Foundation (Grant No. DMS-0811046) and American Chemical Society Petroleum Research Fund (Grant No. 4874-G9). We are indebted to H. Dong and J.F. Morris for experimental data and enlightening discussions.

References

[1] A.K. Gunstensen, D.H. Rothman, S. Zaleski, G. Zanetti, Lattice Boltzmann model for immiscible fluids, Phys. Rev. A 43 (1991) 4320–4327.
[2] X.W. Shan, H.D. Chen, Lattice Boltzmann model for simulating flows with multiple phases and components, Phys. Rev. E 47 (1993) 1815–1819.
[3] M.R. Swift, E. Orlandini, W.R. Osborn, J.M. Yeomans, Lattice Boltzmann simulations of liquid–gas and binary fluid systems, Phys. Rev. E 54 (1996) 5041–5052.
[4] X.Y. He, S.Y. Chen, R.Y. Zhang, A lattice Boltzmann scheme for incompressible multiphase flow and its application in simulation of Rayleigh–Taylor instability, J. Comput. Phys. 152 (1999) 642–663.
[5] T. Inamuro, T. Ogata, S. Tajima, N. Konishi, A lattice Boltzmann method for incompressible two-phase flows with large density differences, J. Comput. Phys. 198 (2004) 628–644.
[6] T. Lee, C.-L. Lin, A stable discretization of the lattice Boltzmann equation for simulation of incompressible two-phase flows at high density ratio, J. Comput. Phys. 206 (2005) 16–47.
[7] H.W. Zheng, C. Shu, Y.T. Chew, A lattice Boltzmann model for multiphase flows with large density ratio, J. Comput. Phys. 218 (2006) 353–371.
[8] P.G. de Gennes, Wetting: statics and dynamics, Rev. Mod. Phys. 57 (1985) 827–863.
[9] R. Benzi, L. Biferale, M. Sbragaglia, S. Succi, F. Toschi, Mesoscopic modeling of a two-phase flow in the presence of boundaries: the contact angle, Phys. Rev. E 74 (2006) 021509.
[10] M. Latva-Kokko, D.H. Rothman, Scaling of dynamic contact angles in a lattice-Boltzmann model, Phys. Rev. Lett. 98 (2007) 254503.
[11] M. Sbragaglia, K. Sugiyama, L. Beferale, Wetting failure and contact line dynamics in a Couette flow, J. Fluid Mech. 614 (2008) 471–493.
[12] Q.M. Chang, J.I.D. Alexander, Analysis of single droplet dynamics on striped surface domains using a lattice Boltzmann method, Microfluid Nanofluid 2 (2006) 309–326.
[13] Y.Y. Yan, Y.Q. Zu, A lattice Boltzmann method for incompressible two-phase flows on partial wetting surface with large density ratio, J. Comput. Phys. 227 (2007) 763–775.
[14] J.W. Cahn, Critical-point wetting, J. Chem. Phys. 66 (1977) 3667–3672.
[15] A.J. Briant, J.M. Yeomans, Lattice Boltzmann simulation of contact line motion: II. Binary fluids, Phys. Rev. E 69 (2004) 031603.
[16] S. Mukherjee, J. Abraham, Investigations of drop impact on dry walls with a lattice-Boltzmann model, J. Colloid Interf. Sci. 312 (2007) 341–354.
[17] R.L. Hoffman, A study of the advancing interface. I. Interface shape in liquid–gas system, J. Colloid Interf. Sci. 50 (1975) 228–241.
[18] S.F. Kistler, Hydrodynamics of wetting, in: J.C. Berg (Ed.), Wettability, Marcel Dekker, New York, 1993, p. 311.
[19] I.V. Roisman, R. Rioboo, C. Tropea, Normal impact of a liquid drop on a dry surface: model for spreading and receding, Proc. R. Soc. Lond. Ser. A 458 (2002) 1411–1430.
[20] Š. Šikalo, H.-D. Wilhelm, I.V. Roisman, S. Jakirlić, C. Tropea, Dynamic contact angle of spreading droplets: experiments and simulations, Phys. Fluids 17 (2005) 062103.
[21] J. Léopoldès, A. Dupuis, D.G. Bucknall, J.M. Yeomans, Jetting micron-scale droplets into chemically heterogeneous surfaces, Langmuir 19 (2003) 9818–9822.
[22] A. Dupuis, J.M. Yeomans, Droplet dynamics on patterned substrates, Langmuir 21 (2005) 2624–2629.
[23] H. Kusumaatmaja, A. Dupuis, J.M. Yeomans, Lattice Boltzmann simulations of drop dynamics, Math. Comput. Simulat. 72 (2006) 160–164.
[24] A.J. Briant, P. Papatzacos, J.M. Yeomans, Lattice Boltzmann simulation of contact line motion in a liquid–gas system, Philos. Trans. R. Soc. Lond. Ser. A 360 (2002) 485–495.

[25] A.J. Briant, A.J. Wagner, J.M. Yeomans, Lattice Boltzmann simulation of contact line motion: I. Liquid–gas systems, Phys. Rev. E 69 (2004) 031602.
[26] T. Lee, L. Liu, Wall boundary conditions in the lattice Boltzmann equation method for non-ideal gases, Phys. Rev. E 78 (2008) 017702.
[27] T. Lee, P.F. Fischer, Eliminating parasitic currents in the lattice Boltzmann equation method for nonideal gases, Phys. Rev. E 74 (2006) 046709.
[28] T. Lee, Effects of incompressibility on the elimination of parasitic currents in the lattice Boltzmann equation method for binary fluids, Comput. Math. Appl. 58 (2009) 987–994.
[29] H. Dong, W.W. Carr, D.G. Bucknall, J.F. Morris, Temporally-resolved inkjet drop impaction on surfaces, AIChE J. 53 (2007) 2606–2617.
[30] F. Capuani, I. Pagonabarraga, D. Frenkel, Discrete solution of the electrokinetic equations, J. Chem. Phys. 121 (2004) 973–986.
[31] H. Ding, P.D.M. Spelt, C. Shu, Diffuse interface model for incompressible two-phase flows with large density ratios, J. Comput. Phys. 226 (2007) 2078–2095.
[32] L. Liu, T. Lee, Wall free energy based polynomial boundary conditions for non-ideal gas lattice Boltzmann equation, Int. J. Mod. Phys. C 20 (2009) 1749–1768.
[33] X.Y. He, L.-S. Luo, A priori derivation of the lattice Boltzmann equation, Phys. Rev. E 55 (1997) R6333.
[34] X.Y. He, S.Y. Chen, G.D. Doolen, A novel thermal model for the lattice Boltzmann method in incompressible limit, J. Comput. Phys. 146 (1998) 282–300.
[35] L.-S. Luo, Unified theory of the lattice Boltzmann models for nonideal gases, Phys. Rev. Lett. 81 (1998) 1618–1621.
[36] Y.-H. Qian, S.-Y. Chen, Dissipative and dispersive behavior of lattice-based models for hydrodynamics, Phys. Rev. E 61 (2000) 2712–2716.
[37] T. Lee, C.-L. Lin, Pressure evolution lattice-Boltzmann-equation method for two-phase flow with phase change, Phys. Rev. E 67 (2003) 056703.
[38] D.B. van Dam, C. Le Clerc, Experimental study of the impact of an ink-jet printed droplet on a solid substrate, Phys. Fluids 16 (2004) 3403–3414.
[39] J. Fukai, Z. Zhao, D. Poulikakos, C.M. Megaridis, O. Miyatake, Modeling of the deformation of a liquid droplet impinging upon a flat surface, Phys. Fluids A 5 (1993) 2588–2599.